Spin and charge density waves in the quasi-one-dimensional KMn_6Bi_5

Jin-Ke Bao[1,2,3], Huibo Cao[4], Matthew J. Krogstad,[1,5] Keith M. Taddei[4], Chenfei Shi[2], Shixun Cao[2,3], Saul H. Lapidus[5], Sander van Smaalen[6], Duck Young Chung[1], Mercouri G. Kanatzidis[1,7], Stephan Rosenkranz[1], Omar Chmaissem[1,8,*]

[1]*Materials Science Division, Argonne National Laboratory, Lemont, Illinois 60439, USA*

[2]*Department of Physics, Materials Genome Institute and International Center for Quantum and Molecular Structures, Shanghai University, Shanghai 200444, China*

[3]*Shanghai Key Laboratory of High Temperature Superconductors, Shanghai University, Shanghai 200444, China*

[4]*Neutron Scattering Division, Oak Ridge National Laboratory, Oak Ridge, Tennessee 37831, USA*

[5]*Advanced Photon Source, Argonne National Laboratory, Lemont, Illinois 60439, USA*

[6]*Laboratory of Crystallography, University of Bayreuth, Bayreuth 95447, Germany*

[7]*Department of Chemistry, Northwestern University, Evanston, Illinois 60208, USA*

[8]*Department of Physics, Northern Illinois University, DeKalb, Illinois 60115, USA*

*Corresponding author: chmaissem@anl.gov

Abstract

The recent observation that pressure could suppress antiferromagnetic (AFM) order in quasi-one-dimensional AMn_6Bi_5 Mn-cluster chains materials (*A* = Na, K, Rb, and Cs) and lead to a superconducting dome offers a new class of materials with which to study unconventional superconductivity. Using neutron diffraction, we elucidate the exact nature of the previously unknown AFM ground state of KMn_6Bi_5 and report finding transverse incommensurate spin density waves (SDWs) for the Mn atoms with a propagating direction along the chains. The SDWs have distinct refined amplitudes of ~2.46 μ_B for the Mn atoms in the pentagons and ~0.29 μ_B with

a large standard deviation for Mn atoms at the center between the pentagons. AFM dominate both the nearest-neighbor Mn-Mn interactions within the pentagon and next-nearest-neighbor Mn-Mn interactions out of the pentagon (along the propagating wave). The SDWs exhibit both local and itinerant characteristics potentially due to cooperative interactions between local magnetic exchange and conduction electrons. Single crystal x-ray diffraction below the AFM transition revealed satellite peaks originating from charge density waves (CDW) along the chain direction with a **q**-vector twice as large as that of the SDW, pointing to a strong real space coupling between them. Additionally, we report a significant magnetoelastic effect during the AFM transition, especially along the chain direction, observed in temperature-dependent x-ray powder diffraction. Our work not only reveals a fascinating intertwined spin, charge, and lattice, orders in one-dimensional KMn_6Bi_5, but also provides an essential piece of information on its magnetic structure to understand the mechanism of superconductivity in this new Mn-based family.

Introduction

In contrast to conventional s-wave electron Cooper pairing predicted by the Bardeen-Cooper-Schrieffer superconductivity theory [1], unconventional superconductors have revealed nontrivial electronic pairing mediated by suppression of the electronic instabilities of a candidate material via chemical substitution or by the application of external pressure [2]. The underlying mechanisms responsible for unconventional superconductivity remain enigmatic despite numerous groundbreaking discoveries of superconducting families like the famous cuprates [3], iron pnictides [4], heavy fermions [5] and organic Bechgaard salts [6].

Unconventional superconductivity has often been associated with various electronic instabilities such as charge or spin density waves (CDW or SDW), with the competing orders providing a fascinating opportunity to combine widely distinct physical phenomena and create new electronic landscapes. The original observation of a static stripe phase in $La_{1.6-x}Nd_{0.4}Sr_xCuO_4$ [7], in which coexisting SDW and CDW were suggested to correlate with the anomalous suppression of superconductivity, opened the door to extensive experimental and theoretical research that ultimately established the dependence of hole-doped cuprates' superconductivity on intertwined symmetry-breaking long-range or short-range electronic and

magnetic correlations [8–27]. Curiously and to the best of our knowledge, coexistence of the SDW and CDW orders has not been observed in other superconducting families, thus, highlighting the urgent need for new materials in which both orders are present and leading to superconductivity.

Superconductivity was recently reported in a series of Mn-based Q1D AMn$_6$Bi$_5$ (A = K, Rb and Cs) materials [28–30] via the suppression of their AFM orders under 9-15 GPa external pressures [30–32]. AMn$_6$Bi$_5$ is a model system that offers a rare opportunity for investigations of electronic instabilities in a nuclear structure which consists of unique [Mn$_6$Bi$_5$]$^-$ nanowires with counterions A intercalated in between to form a Q1D crystal structure [28,29,33,34], see Figure 1(a,b). Considering the similar phase diagrams of unconventional superconductivity tuned by high pressure [2,35–37], it is reasonable to classify AMn$_6$Bi$_5$ as another class of unconventional superconductors whose underlying physics must be uncovered. Moreover, Q1D systems in which electron-electron correlations and quantum fluctuations become enhanced due to the quantum confinement of electrons [38], are expected to enrich the physics of this superconducting family through various mechanisms. For example, collective electronic instabilities in Q1D systems gave rise to spin-charge separated Tomonaga-Luttinger liquids [39], CDW [40,41], SDW [42,43] and unconventional superconductivity with spin-triplet pairing [44–49].

The magnetic ground state of this emerging family of AMn$_6$Bi$_5$ superconductors has remained until now unknown, thus, significantly hindering the ability to properly consider potential pairing interactions and to make meaningful comparisons with the broader family of unconventional superconductors. In the present work, we use neutron single crystal diffraction to solve this conundrum, demonstrating the formation of multiple AFM amplitude-modulated SDW in KMn$_6$Bi$_5$. Moreover, using x-ray single crystal diffraction, we discovered a CDW with a propagation vector twice as large as that of the SDW. The observation of CDW in coexistence with SDW as a prelude to superconductivity in KMn$_6$Bi$_5$ is of paramount importance since it offers a system to the condensed matter community second only to the hole-doped cuprate superconductors. Our discovery will enable further studies to elucidate the nature of the intertwined orders in diverse AMn$_6$Bi$_5$ solid solutions where A is tuned by various mixtures of the alkali metals.

Experimental Details

The preparation methods of samples for neutron and x-ray diffraction are described in Supplemental Material (SM) [50] (see, also, reference [1] therein). Synchrotron powder and single crystal x-ray diffraction were performed at beamline 11-BM-B and 6-ID-D of the Advanced Photon Source at Argonne National Laboratory (ANL), respectively. Magnetic structure determination and order parameter scans were performed using neutron powder diffraction at beamline HB-2A and neutron single crystal diffraction at beamline HB-3A [51] at the high flux isotope reactor (HFIR) at Oak Ridge National Laboratory (ORNL). Data collection details, processing and analysis are provided in the SM [50] (see, also, references [2-7] therein). Crystal and magnetic structures were plotted using the software VESTA [52].

Results and discussion

Structural Properties

KMn_6Bi_5 crystallizes in a monoclinic crystal structure (No. 12, *C*2/*m*) consisting of two $[Mn_6Bi_5]^-$ in one unit cell [28], see Figure 1(a). Each $[Mn_6Bi_5]^-$ nanowire can be decomposed into a chain of corner-shared Mn-centered icosahedral clusters (13 Mn atoms) encapsulated inside a Bi nanotube, see Figure 1(b). The Mn clusters consist of five independent Mn sites (Mn1 – Mn5) that form two flat pentagons lying within the *ac* planes, at *y*-coordinates of 0 and 0.5, with an additional independent Mn6 site (referred to as central Mn) occupying central positions, at *y*-coordinates of 0.25 and 0.75, between any two adjacent pentagons stacked along the *b*-axis. The Mn pentagons are structurally related via the symmetry operators of the monoclinic *C*2/*m* space group. No sign of any structural symmetry transformation was detected across its AFM transition from temperature-dependent x-ray powder diffraction measurements. The temperature-dependent behavior of the diffraction data agrees with an overall positive thermal expansion of the material and the anomalies at ~75 K (the opposite responses of the peaks (10 0 –3) and (0 2 0) during the transition) imply significant anisotropic magnetoelastic coupling between its crystal lattice and magnetic order [53,54], Figure 1(c). Additional peaks are tracked as shown in Figure S1 [50].

Quantitative temperature-dependent lattice parameters of KMn_6Bi_5 determined from Rietveld refinements are shown in Figure 1(d). With the exception of a subtle slope change of the unit cell volume, all the lattice parameters display a clear anomaly at ~75 K. It is worth emphasizing the rapidly decreasing lattice parameter *b* after the system enters the AFM state, which is ascribed to strong AFM exchange magnetostriction [55] within the Mn cluster chains as described below. In contrast, the *a* and *c* lattice parameters both exhibit a smaller increase just below the paramagnetic to antiferromagnetic phase transition.

Given that the interchain magnetic interactions are much weaker than their intrachain counterparts, one can argue that the negative thermal expansion displayed by *a* and *c* results from elastic strains produced by compression of the lattice along the chain direction (*i.e.*, the *b*-axis). On the other hand, the relatively larger positive thermal expansion along the *b*-axis, Figure 1(d), suggests that one-dimensional magnetic interactions along the chain direction play a dominant role in determining the overall magnetoelastic properties of the material below 99 K.

Incommensurate Spin Density Waves (ISDW)

To determine the magnetic structure of KMn_6Bi_5, single crystal neutron diffraction was performed. The high quality of our single crystal is demonstrated by the excellent goodness-of-fit and agreement factors obtained at 4 K for the refined nuclear structure as shown in Figure S2(a) and Table S1 in the SM [50]. Reciprocal space scans revealed the existence of a new set of reflections of magnetic origin at temperatures below 75 K, which we successfully indexed using an incommensurate propagation vector $\mathbf{q_s}$ = (1, 0.418, 0). This result is markedly different from any of the theoretical commensurate magnetic models proposed by Chen *et al.* [29] and likely indicates a complex energy landscape with numerous competing magnetic interactions. An order parameter scan was performed using the magnetic reflection (1 0.418 1) and gave a fitted critical component β of 0.15(3) for KMn_6Bi_5 (Figure S2(c) in SM [[50]) (see, also, references [9-10] therein), typical of systems with reduced dimensionality and much smaller than the theoretical value of 0.37 for three-dimensional Heisenberg systems [56], which agrees well with the proposed Q1D magnetic interactions [57,58].

Given the incommensurate **q**-vector hosted by a monoclinic structure in which 6 independent Mn sites describe a total of 24 Mn ions per unit cell, one would expect the resulting magnetic structure to be of low symmetry. To start, we considered the highest symmetry magnetic models each of which had the same 6 symmetry distinct Mn sites as the nuclear structure, however, in our modeling we found it necessary to go beyond these structures and further break the *C*-centering symmetry to obtain reasonable agreement with the observed intensities. This symmetry breaking increased the number of independent Mn sites to 12 per unit cell, see Figures 2 and 3 and magnetic modeling in SM [50]. In our final model with an agreement factor of about 8% (Figure S2(b)), amplitude modulated SDWs with a period of about twelve-unit cells (~55.4 Å) along the *b* axis are observed. The 2-fold rotation symmetry along the (0.5, *y*, 0.5) axis transforms the magnetic moments (*u*, 0, *w*) of Mn atoms in one Mn-cluster chain to (-*u*, 0, -*w*) of Mn atoms in the other Mn-cluster chain as shown in Figure 3. Each one Mn-atom chain (with a Mn-Mn distance equal to that of the lattice parameter of *b*) has an independent SDW. For the central Mn sites (Mn6 and Mn12 with *b*/2 Mn-Mn distance), two separate waves are superimposed. We note that the waves passing through the basal pentagons (*i.e.*, at $y = 0$) are ahead of the waves that propagate through the Mn pentagons at $y = 0.5$ by about 284°. This phase shift determined by the strong coupling of SDWs between two neighboring Mn pentagons within the same Mn-cluster chain is likely the driving force leading to breaking the *C*-centering of the parent space group. Other models such as spiral helical magnetic ones were tried, however, they either inadequately modeled the data or else converged to the current solution, see refinement details in SM [50](see, also, reference [8] therein). Our model produces an excellent fit to the magnetic intensities observed by neutron powder diffraction data collected at 3 K (Figure S3).

The above-described structure has 12 independent SDWs on the Mn atoms coupled and propagated together along one single Mn-cluster chain in KMn_6Bi_5. The magnetic configuration can be described by the general formula [59]:

$$\mathbf{m_{ji}} = \mathbf{m_i}\cos(-2\pi\mathbf{q_s}\cdot\mathbf{R_j} + \varphi_i)\ (i = 1\text{-}24)$$

Where $\mathbf{m_{ji}}$ and $\mathbf{m_i}$ with a vector form of (*u*, 0, *w*) are the magnetic moments in the *j*th unit cell and wave amplitudes for the Mn*i* atom, respectively, $\mathbf{R_j}$ is the translation vector, $\mathbf{q_s}$ is the propagation vector and φ_i is the phase for one certain Mn atom. The magnetic moments and directions of Mn6

and Mn12 cannot be determined accurately from our current dataset due to the majority of the magnetic scattering coming from the Mn pentagons which exhibit significantly larger magnetic moments. For clarity, the waves from different Mn pentagons are separated as shown in Figure 3(a,b). The refined magnetic structure parameters are presented in Table S2 in SM [50]. It is important to note that in our model the Mn magnetic moments oscillate along the chain direction, in stark contrast to the predicted helical magnetic model by Chen *et al.* [29] where they are constant along the chain direction, but their directions vary.

All the SDWs along the chain are transverse in KMn_6Bi_5 since the propagating direction is perpendicular to the spin direction. In a conventional transverse SDW, the modulated magnetic moments point in one direction for half of the wave then reverse direction in the other half as in Cr metal [60], for example. In this work, the component of the vector $\mathbf{q_s}$ along the chain direction is 0.418 which corresponds to a phase shift of 150° when moving one unit cell along the chain direction. As a result, the magnetic moments are not only modulated in magnitude as expected for a transverse SDW but also coupled antiferromagnetically between neighboring Mn sites along the wave direction – an unusual configuration which will be discussed later.

SDW instabilities can arise in a low-dimensional metallic system due to electron-electron interactions [61], which is consistent with the metallic 3d transition metal Q1D KMn_6Bi_5. Indeed, carrier concentration decreases during the AFM transition probably ascribed to partial gapping of the Fermi surface [28]. The determination of Fermi surface in KMn_6Bi_5 will be essential to probe if Fermi surface nesting is the major driving force triggering its SDW instability and consequently to understand its impact on superconductivity. A simple calculation of the oxidation state reveals that a total of +14 charges must be accounted for by the six Mn ions assuming K^+ and Bi^{3-} [62]. Our refinements of ~2.46 μ_B and 0.29 μ_B as the wave magnitudes and their corresponding root mean square values of 1.73 and 0.21 μ_B for the pentagon and central Mn atoms, respectively, suggest possible charge disproportionation and ordering of the different magnetic moments with five Mn^{2+} (5 μ_B for high spin) making the pentagons and one Mn^{4+} (1 μ_B for low spin) along the pentagon axes. The reduced magnetic moment of Mn in KMn_6Bi_5 can be realized by delocalization of the 3d electrons from Mn-Mn metallic bonding within the chain [28]. The significantly smaller

magnetic moment in the central Mn ions is supported by the very short Mn-Mn distance (~ 2.28 Å at 4 K) where strong metallic bonding between Mn atoms exists [63]. First-principles calculations on *A*Mn_6Bi_5 do reveal that Mn-3d electrons dominate the density of states around the Fermi level, proving the itineracy of the 3d electrons [29,33]. The small magnetic moments obtained in the model are also nominally consistent with the small effective magnetic moment per Mn atom obtained from the Curie-Weiss fitting [28,31]. The disproportionation of magnetic moments of Mn atoms in KMn_6Bi_5 is reminiscent of the coexistence of magnetic (2-3 μ_B) and almost nonmagnetic (0.2-0.6 μ_B) Mn atoms in the allotrope α-Mn [64]. Our results agree well with DFT calculations performed by Chen *et al*. [29] from which the central Mn ions are found to have a much smaller magnetic moment than the pentagon Mn. The small magnetic moments in KMn_6Bi_5 may be key to achieving superconductivity by high pressures like CrAs [35] and MnP [36] where fragile AFM can be easily quenched.

While the small effective magnetic moments from central Mn atoms (0.21 μ_B) are similar to those of a typical SDW system [3,6,65], the effective magnetic moments (1.73 μ_B) of Mn in the pentagon in KMn_6Bi_5 are relatively large, indicating that magnetism comes from both localized and itinerant electrons as in GdSi, for example, where local magnetic moments and itinerant electrons form a cooperative magnetic configuration [66]. In terms of a local magnetic picture, the Mn-Bi-Mn magnetic exchange geometry in KMn_6Bi_5 is similar to that in the prototypical insulator $BaMn_2Bi_2$ where AFM coupling dominates both nearest and next-nearest neighboring Mn-Mn interactions [67]. The canted AFM configuration for two nearest-neighbor Mn atoms in the pentagon in KMn_6Bi_5 can therefore be explained as a compromise arising from geometric frustration and AFM exchange coupling via Bi atoms in the same plane, see Figure 2. AFM coupling in the waves for Mn pentagons can be understood by next-nearest-neighbor Mn-Mn magnetic exchange using Bi atoms sandwiched between them as a bridge [29]. In contrast to other pressure-induced superconductors containing 3d electrons such as CrAs [35] and MnP [36] with some degree of ferromagnetic interactions, AFM dominates in KMn_6Bi_5 with a one-dimensional and strongly coupled magnetic sublattice, which poses a constraint on creating a theoretical model to understand its superconductivity under high pressure.

Incommensurate Charge Density Waves (ICDW)

In addition to single crystal neutron diffraction, we performed single crystal synchrotron x-ray diffraction which surprisingly revealed the existence of satellite reflections, in addition to the main Bragg peaks below the magnetic phase transition (at 30 K), as shown in Figure 4. These extra peaks can be successfully indexed using a propagation vector $\mathbf{q_c} \approx (0, 0.83, 0)$, suggesting the existence of a CDW along the chain direction. The charge propagation vector $\mathbf{q_c}$ is almost double that of the incommensurate modulated component of the SDW vector $\mathbf{q_s}$ indicating their strong coupling in real space as is also observed for example in Cr [60,68], underdoped cuprates [69] and nickelates [70]. *C*-centering symmetry in the crystal structure is still preserved at 30 K based on the rule of the extinction condition for the main reflections despite it being broken by the magnetic structure. Integrated synchrotron intensities at 30 and 297 K are shown in Figure S4 and S5 in SM [50].

Compared to the SDW, the CDW is more subtle in KMn_6Bi_5, pointing to a second-order-effect consequence of SDW. No additional anomalies related to the CDW order can be identified in resistance, magnetic susceptibility, or heat capacity measurements. One possible scenario may relate the CDW to magnetostriction effects between neighboring magnetic moments which result in a charge modulation period equal to half of the spin modulation period in the real space since it does not depend on the directions of those neighboring moments [71]. An incommensurate superspace-group structure refinement is essential to resolve the detailed charge modulation, which, however, cannot be carried out due to the limited quality of the current dataset.

Conclusions

Using a combination of neutron and synchrotron x-ray scattering, we successfully determined the coexistence of complex incommensurate charge and spin density waves in KMn_6Bi_5. Out-of-phase incommensurate SDW with sizeable magnitudes of about 2.46 μ_B propagate through the Mn pentagons along the *b*-axis direction. In contrast, waves with a small magnitude of no more than 0.29 μ_B pass through the central Mn chain. The magnetism in KMn_6Bi_5 has the dichotomy of both

local and itinerant characteristics. AFM interactions dominate both within the Mn pentagons and out of the pentagons along the waves in KMn_6Bi_5. The Mn-cluster chains are antiferromagnetically and ferromagnetically coupled along the *a* and *c* axis, respectively. The reduced magnetic moments of Mn in KMn_6Bi_5 are believed to be an important ingredient to quench the fragile AFM order and achieve superconductivity under high pressure. The CDW found in this work is much subtler than the SDW and probably originates from a magnetostriction effect of the SDW indicating a strong coupling between the two instabilities [71]. KMn_6Bi_5, as a unique Q1D system, demonstrates strong interactions among different degrees of freedom such as spin, charge, and lattice. The intertwined orders, including SDW, its induced CDW at ambient pressure and superconductivity under high pressure in KMn_6Bi_5 provide a fascinating playground to develop microscopic theories to explain the origins of these quantum phases and their intimate interplay with the potential for complicated landscapes as in the superconducting cuprates [72].

Acknowledgements

This work was supported by the U.S. Department of Energy, Office of Science, Basic Energy Sciences, Materials Sciences and Engineering Division. This research used resources of the Advanced Photon Source; a U.S. Department of Energy (DOE) Office of Science User Facility operated for the DOE Office of Science by Argonne National Laboratory under Contract No. DE-AC02-06CH11357. This research used resources at the High Flux Isotope Reactor, the DOE Office of Science User Facility operated by ORNL. J.-K. Bao acknowledges support from the Natural Science Foundation of China (Grant No. 12204298). The authors thank Prof. Guang-Han Cao for insightful discussions and Dr. Daniel Phelan for reading and commenting on the manuscript.

References

[1] J. Bardeen, L. N. Cooper, and J. R. Schrieffer, *Theory of Superconductivity*, Physical Review **108**, 1175 (1957).

[2] M. R. Norman, *The Challenge of Unconventional Superconductivity*, Science (1979) **332**, 196 (2011).

[3] B. Keimer, S. A. Kivelson, M. R. Norman, S. Uchida, and J. Zaanen, *From Quantum Matter to High-Temperature Superconductivity in Copper Oxides*, Nature **518**, 179 (2015).

[4] J. Paglione and R. L. Greene, *High-Temperature Superconductivity in Iron-Based Materials*, Nat Phys **6**, 645 (2010).

[5] N. D. Mathur, F. M. Grosche, S. R. Julian, I. R. Walker, D. M. Freye, R. K. W. Haselwimmer, and G. G. Lonzarich, *Magnetically Mediated Superconductivity in Heavy Fermion Compounds*, Nature **394**, 39 (1998).

[6] D. Jaccard, H. Wilhelm, D. Jérome, J. Moser, C. Carcel, and J. M. Fabre, *From Spin-Peierls to Superconductivity: $(TMTTF)_2PF_6$ under High Pressure*, Journal of Physics: Condensed Matter **13**, L89 (2001).

[7] J. M. Tranquada, B. J. Sternlieb, J. D. Axe, Y. Nakamura, and S. Uchida, *Evidence for Stripe Correlations of Spins and Holes in Copper Oxide Superconductors*, Nature **375**, 561 (1995).

[8] J. M. Tranquada, P. Wochner, and D. J. Buttrey, *Spin Dynamics in an Ordered Stripe Phase*, Phys Rev Lett **79**, 2133 (1997).

[9] J. M. Tranquada, J. D. Axe, N. Ichikawa, A. R. Moodenbaugh, Y. Nakamura, and S. Uchida, *Coexistence of, and Competition between, Superconductivity and Charge-Stripe Order in $La_{1.6-x}Nd_{0.4}Sr_xCuO_4$*, Phys Rev Lett **78**, 338 (1997).

[10] N. Ichikawa, S. Uchida, J. M. Tranquada, T. Niemöller, P. M. Gehring, S.-H. Lee, and J. R. Schneider, *Local Magnetic Order vs Superconductivity in a Layered Cuprate*, Phys Rev Lett **85**, 1738 (2000).

[11] S. Wakimoto, J. M. Tranquada, T. Ono, K. M. Kojima, S. Uchida, S. H. Lee, P. M. Gehring, and R. J. Birgeneau, *Diagonal Static Spin Correlation in the Low-Temperature Orthorhombic Pccn Phase of $La_{1.55}Nd_{0.4}Sr_{0.05}CuO_4$*, Phys Rev B Condens Matter Mater Phys **64**, 174505 (2001).

[12] C. Niedermayer, C. Bernhard, T. Blasius, A. Golnik, A. Moodenbaugh, and J. I. Budnick, *Common Phase Diagram for Antiferromagnetism in $La_{2-x}Sr_xCuO_4$ and $Y_{1-x}Ca_xBa_2Cu_3O_6$ as Seen by Muon Spin Rotation*, Phys Rev Lett **80**, 3843 (1998).

[13] T. Suzuki, T. Goto, K. Chiba, T. Shinoda, T. Fukase, H. Kimura, K. Yamada, M. Ohashi, and Y. Yamaguchi, *Observation of Modulated Magnetic Long-Range Order in $La_{1.88}Sr_{0.12}CuO_4$*, Phys Rev B **57**, R3229 (1998).

[14] M. Matsuda, Y. S. Lee, M. Greven, M. A. Kastner, R. J. Birgeneau, K. Yamada, Y. Endoh, P. Böni, S.-H. Lee, S. Wakimoto, et al., *Freezing of Anisotropic Spin Clusters in $La_{1.98}Sr_{0.02}CuO_4$*, Phys Rev B **61**, 4326 (2000).

[15] Y. S. Lee, R. J. Birgeneau, M. A. Kastner, Y. Endoh, S. Wakimoto, K. Yamada, R. W. Erwin, S.-H. Lee, and G. Shirane, *Neutron-Scattering Study of Spin-Density Wave Order in the Superconducting State of Excess-Oxygen-Doped La_2CuO_{4+y}*, Phys Rev B **60**, 3643 (1999).

[16] H. A. Mook, P. Dai, and F. Doğan, *Charge and Spin Structure in $YBa_2Cu_3O_{6.35}$*, Phys Rev Lett **88**, 097004 (2002).

[17] G. Ghiringhelli, M. le Tacon, M. Minola, S. Blanco-Canosa, C. Mazzoli, N. B. Brookes, G. M. de Luca, A. Frano, D. G. Hawthorn, F. He, et al., *Long-Range Incommensurate Charge Fluctuations in (Y,Nd)$Ba_2Cu_3O_{6+x}$*, Science (1979) **337**, 821 (2012).

[18] J. Li, A. Nag, J. Pelliciari, H. Robarts, A. Walters, M. Garcia-Fernandez, H. Eisaki, D. Song, H. Ding, S. Johnston, et al., *Multiorbital Charge-Density Wave Excitations and Concomitant Phonon Anomalies in $Bi_2Sr_2LaCuO_{6+\delta}$*, Proceedings of the National Academy of Sciences **117**, 16219 (2020).

[19] P. Abbamonte, A. Rusydi, S. Smadici, G. D. Gu, G. A. Sawatzky, and D. L. Feng, *Spatially Modulated "Mottness" in $La_{2-x}Ba_xCuO_4$*, Nat Phys **1**, 155 (2005).

[20] T. Wu, H. Mayaffre, S. Krämer, M. Horvatić, C. Berthier, W. N. Hardy, R. Liang, D. A. Bonn, and M.-H. Julien, *Magnetic-Field-Induced Charge-Stripe Order in the High-Temperature Superconductor $YBa_2Cu_3O_y$*, Nature **477**, 191 (2011).

[21] J. Chang, E. Blackburn, A. T. Holmes, N. B. Christensen, J. Larsen, J. Mesot, R. Liang, D. A. Bonn, W. N. Hardy, A. Watenphul, et al., *Direct Observation of Competition between Superconductivity and Charge Density Wave Order in $YBa_2Cu_3O_{6.67}$*, Nat Phys **8**, 871 (2012).

[22] R. Comin, A. Frano, M. M. Yee, Y. Yoshida, H. Eisaki, E. Schierle, E. Weschke, R. Sutarto, F. He, A. Soumyanarayanan, et al., *Charge Order Driven by Fermi-Arc Instability in $Bi_2Sr_{2-x}La_xCuO_{6+\delta}$*, Science (1979) **343**, 390 (2014).

[23] E. H. da Silva Neto, P. Aynajian, A. Frano, R. Comin, E. Schierle, E. Weschke, A. Gyenis, J. Wen, J. Schneeloch, Z. Xu, et al., *Ubiquitous Interplay Between Charge Ordering and High-Temperature Superconductivity in Cuprates*, Science (1979) **343**, 393 (2014).

[24] W. Tabis, Y. Li, M. le Tacon, L. Braicovich, A. Kreyssig, M. Minola, G. Dellea, E. Weschke, M. J. Veit, M. Ramazanoglu, et al., *Charge Order and Its Connection with Fermi-Liquid Charge Transport in a Pristine High-Tc Cuprate*, Nat Commun **5**, 5875 (2014).

[25] T. P. Croft, C. Lester, M. S. Senn, A. Bombardi, and S. M. Hayden, *Charge Density Wave Fluctuations in $La_{2-x}Sr_xCuO_4$ and Their Competition with Superconductivity*, Phys Rev B **89**, 224513 (2014).

[26] R. Comin and A. Damascelli, *Resonant X-Ray Scattering Studies of Charge Order in Cuprates*, Annu Rev Condens Matter Phys **7**, 369 (2016).

[27] R. Arpaia, S. Caprara, R. Fumagalli, G. de Vecchi, Y. Y. Peng, E. Andersson, D. Betto, G. M. de Luca, N. B. Brookes, F. Lombardi, et al., *Dynamical Charge Density Fluctuations Pervading the Phase Diagram of a Cu-Based High*-T_c *Superconductor*, Science (1979) **365**, 906 (2019).

[28] J.-K. Bao, Z.-T. Tang, H. J. Jung, J.-Y. Liu, Y. Liu, L. Li, Y.-K. Li, Z.-A. Xu, C.-M. Feng, H. Chen, et al., *Unique $[Mn_6Bi_5]^-$ Nanowires in KMn_6Bi_5: A Quasi-One-Dimensional Antiferromagnetic Metal*, J Am Chem Soc **140**, 4391 (2018).

[29] L. Chen, L. Zhao, X. Qiu, Q. Zhang, K. Liu, Q. Lin, and G. Wang, *Quasi-One-Dimensional Structure and Possible Helical Antiferromagnetism of $RbMn_6Bi_5$*, Inorg Chem **60**, 12941 (2021).

[30] S. Long, L. Chen, Y. Wang, Y. Zhou, S. Cai, J. Guo, Y. Zhou, K. Yang, S. Jiang, Q. Wu, et al., *Flipping of Antiferromagnetic to Superconducting States in Pressurized Quasi-One-Dimensional Manganese-Based Compounds*, ArXivID:2207.14697 (2022).

[31] Z. Y. Liu, Q. X. Dong, P. T. Yang, P. F. Shan, B. S. Wang, J. P. Sun, Z. L. Dun, Y. Uwatoko, G. F. Chen, X. L. Dong, et al., *Pressure-Induced Superconductivity up to 9 K in the Quasi-One-Dimensional KMn_6Bi_5*, Phys Rev Lett **128**, 187001 (2022).

[32] P.-T. Yang, Q.-X. Dong, P.-F. Shan, Z.-Y. Liu, J.-P. Sun, Z.-L. Dun, Y. Uwatoko, G.-F. Chen, B.-S. Wang, and J.-G. Cheng, *Emergence of Superconductivity on the Border of Antiferromagnetic Order in $RbMn_6Bi_5$ under High Pressure: A New Family of Mn-Based Superconductors*, Chin. Phys. Lett. **39**, 067401 (2022).

[33] Y. Zhou, L. Chen, G. Wang, Y.-X. Wang, Z.-C. Wang, C.-C. Chai, Z.-N. Guo, J.-P. Hu, and X.-L. Chen, *A New Superconductor Parent Compound $NaMn_6Bi_5$ with Quasi-One-Dimensional Structure and Lower Antiferromagnetic-Like Transition Temperatures*, Chinese Physics Letters **39**, 047401 (2022).

[34] H. J. Jung, J.-K. Bao, D. Y. Chung, M. G. Kanatzidis, and V. P. Dravid, *Unconventional Defects in a Quasi-One-Dimensional KMn_6Bi_5*, Nano Lett **19**, 7476 (2019).

[35] W. Wu, J. Cheng, K. Matsubayashi, P. Kong, F. Lin, C. Jin, N. Wang, Y. Uwatoko, and J. Luo, *Superconductivity in the Vicinity of Antiferromagnetic Order in CrAs*, Nat Commun **5**, 5508 (2014).

[36] J.-G. Cheng, K. Matsubayashi, W. Wu, J. P. Sun, F. K. Lin, J. L. Luo, and Y. Uwatoko, *Pressure Induced Superconductivity on the Border of Magnetic Order in MnP*, Phys Rev Lett **114**, 117001 (2015).

[37] T. L. Hung, C. H. Huang, L. Z. Deng, M. N. Ou, Y. Y. Chen, M. K. Wu, S. Y. Huyan, C. W. Chu, P. J. Chen, and T. K. Lee, *Pressure Induced Superconductivity in MnSe*, Nat Commun **12**, 5436 (2021).

[38] T. Giamarchi, *Theoretical Framework for Quasi-One Dimensional Systems*, Chem Rev **104**, 5037 (2004).

[39] J. Voit, *One-Dimensional Fermi Liquids*, Reports on Progress in Physics **58**, 977 (1995).

[40] G. Grüner, *The Dynamics of Charge-Density Waves*, Rev Mod Phys **60**, 1129 (1988).

[41] J. P. Pouget, S. Ravy, and B. Hennion, *The Charge-Density Wave Instability in Quasi One-Dimensional Conductors*, Phase Transitions **30**, 5 (1991).

[42] D. Jérome, *The Physics of Organic Superconductors*, Science (1979) **252**, 1509 (1991).

[43] G. Grüner, *The Dynamics of Spin-Density Waves*, Rev Mod Phys **66**, 1 (1994).

[44] Y. Zhou, C. Cao, and F.-C. Zhang, *Theory for Superconductivity in Alkali Chromium Arsenides A2Cr3As3 (A = K, Rb, Cs)*, Sci Bull (Beijing) **62**, 208 (2017).

[45] X. Wu, F. Yang, C. Le, H. Fan, and J. Hu, *Triplet p_z -Wave Pairing in Quasi-One-Dimensional $A_2Cr_3As_3$ Superconductors (A = K, Rb, Cs)*, Phys Rev B **92**, 104511 (2015).

[46] J. Yang, J. Luo, C. Yi, Y. Shi, Y. Zhou, and G. Zheng, *Spin-Triplet Superconductivity in $K_2Cr_3As_3$*, Sci Adv **7**, eabl4432 (2021).

[47] K. M. Taddei, B.-H. Lei, M. A. Susner, H.-F. Zhai, T. J. Bullard, L. D. Sanjeewa, Q. Zheng, A. S. Sefat, S. Chi, C. dela Cruz, et al., *Gapless Spin-Excitations in the Superconducting State of a Quasi-One-Dimensional Spin-Triplet Superconductor*, ArXiv:2206.11757 (2022).

[48] S. Reja and S. Nishimoto, *Triplet Superconductivity in Coupled Odd-Gon Rings*, Sci Rep **9**, 2691 (2019).

[49] J.-K. Bao, J.-Y. Liu, C.-W. Ma, Z.-H. Meng, Z.-T. Tang, Y.-L. Sun, H.-F. Zhai, H. Jiang, H. Bai, C.-M. Feng, et al., *Superconductivity in Quasi-One-Dimensional $K_2Cr_2As_3$ with Significant Electron Correlations*, Phys Rev X **5**, 011013 (2015).

[50] *See Supplemental Material at [URL Will Be Inserted by Publisher] for Additional Information on Experimental Details, Neutron Powder Diffraction, and Synchrotron X-Ray Single Crystal Diffraction*.

[51] H. Cao, B. Chakoumakos, K. Andrews, Y. Wu, R. Riedel, J. Hodges, W. Zhou, R. Gregory, B. Haberl, J. Molaison, et al., *DEMAND, a Dimensional Extreme Magnetic Neutron Diffractometer at the High Flux Isotope Reactor*, Crystals (Basel) **9**, 5 (2018).

[52] K. Momma and F. Izumi, VESTA 3 *for Three-Dimensional Visualization of Crystal, Volumetric and Morphology Data*, J Appl Crystallogr **44**, 1272 (2011).

[53] J. Angelkort, A. Wölfel, A. Schönleber, S. van Smaalen, and R. K. Kremer, *Observation of Strong Magnetoelastic Coupling in a First-Order Phase Transition of CrOCl*, Phys Rev B **80**, 144416 (2009).

[54] T. Kimura, Y. Tomioka, A. Asamitsu, and Y. Tokura, *Anisotropic Magnetoelastic Phenomena in Layered Manganite Crystals: Implication of Change in Orbital State*, Phys Rev Lett **81**, 5920 (1998).

[55] N. Narayanan, A. Senyshyn, D. Mikhailova, T. Faske, T. Lu, Z. Liu, B. Weise, H. Ehrenberg, R. A. Mole, W. D. Hutchison, et al., *Magnetic Structure and Spin Correlations in Magnetoelectric Honeycomb $Mn_4Ta_2O_9$*, Phys Rev B **98**, 134438 (2018).

[56] T. Chatterji, *Neutron Scattering from Magnetic Materials* (Elsevier, Amsterdam, 2006).

[57] M. Fujihala, S. Mitsuda, R. A. Mole, D. H. Yu, I. Watanabe, S. Yano, T. Kuwai, H. Sagayama, T. Kouchi, H. Kamebuchi, et al., *Spin Dynamics and Magnetic Ordering in the Quasi-One-Dimensional S=1/2 Antiferromagnet $Na_2CuSO_4Cl_2$*, Phys Rev B **101**, 024410 (2020).

[58] S. K. Karna, D. Tristant, J. K. Hebert, G. Cao, R. Chapai, W. A. Phelan, Q. Zhang, Y. Wu, C. Dhital, Y. Li, et al., *Helical Magnetic Order and Fermi Surface Nesting in Noncentrosymmetric ScFeGe*, Phys Rev B **103**, 014443 (2021).

[59] A. Wills, *Magnetic Structures and Their Determination Using Group Theory*, Le Journal de Physique IV **11**, Pr9 (2001).

[60] E. Fawcett, *Spin-Density-Wave Antiferromagnetism in Chromium*, Rev Mod Phys **60**, 209 (1988).

[61] G. Grüner, *Density Waves in Solids*, Vol. CRC Press (CRC Press, 2018).

[62] K. H. Whitmire, *Encyclopedia of Inorganic and Bioinorganic Chemistry* (n.d.).

[63] A. Pandey, P. Miao, M. Klemm, H. He, H. Wang, X. Qian, J. W. Lynn, and M. C. Aronson, *Correlations and Incipient Antiferromagnetic Order within the Linear Mn Chains of Metallic Ti_4MnBi_2*, Phys Rev B **102**, 014406 (2020).

[64] T. Yamada, N. Kunitomi, Y. Nakai, D. E. Cox, and G. Shirane, *Magnetic Structure of α-Mn*, J Physical Soc Japan **28**, 615 (1970).

[65] W. Bao, C. Broholm, S. A. Carter, T. F. Rosenbaum, G. Aeppli, S. F. Trevino, P. Metcalf, J. M. Honig, and J. Spalek, *Incommensurate Spin Density Wave in Metallic $V_{2-y}O_3$*, Phys Rev Lett **71**, 766 (1993).

[66] Y. Feng, J. Wang, D. M. Silevitch, B. Mihaila, J. W. Kim, J.-Q. Yan, R. K. Schulze, N. Woo, A. Palmer, Y. Ren, et al., *Incommensurate Antiferromagnetism in a Pure Spin System via Cooperative Organization of Local and Itinerant Moments*, Proceedings of the National Academy of Sciences **110**, 3287 (2013).

[67] S. Calder, B. Saparov, H. B. Cao, J. L. Niedziela, M. D. Lumsden, A. S. Sefat, and A. D. Christianson, *Magnetic Structure and Spin Excitations in $BaMn_2Bi_2$*, Phys Rev B **89**, 064417 (2014).

[68] Y. Hu, T. Zhang, D. Zhao, C. Chen, S. Ding, W. Yang, X. Wang, C. Li, H. Wang, D. Feng, et al., *Real-Space Observation of Incommensurate Spin Density Wave and Coexisting Charge Density Wave on Cr (001) Surface*, Nat Commun **13**, 445 (2022).

[69] J. M. Tranquada, *Cuprate Superconductors as Viewed through a Striped Lens*, Adv Phys **69**, 437 (2020).

[70] J. Zhang, D. Phelan, A. S. Botana, Y.-S. Chen, H. Zheng, M. Krogstad, S. G. Wang, Y. Qiu, J. A. Rodriguez-Rivera, R. Osborn, et al., *Intertwined Density Waves in a Metallic Nickelate*, Nat Commun **11**, 6003 (2020).

[71] G. van der Laan and I. H. Munro, *X-Ray Scattering and Absorption by Magnetic Materials. By S. W. Lovesey and S. P. Collins (Oxford Series on Synchrotron Radiation, No. 1). Pp. 390. Clarendon Press, 1996. Price (Hardback) £70.00. ISBN 0-19-851737-8.*, J Synchrotron Radiat **5**, 1181 (1998).

[72] E. Fradkin, S. A. Kivelson, and J. M. Tranquada, *Colloquium: Theory of Intertwined Orders in High Temperature Superconductors*, Rev Mod Phys **87**, 457 (2015).

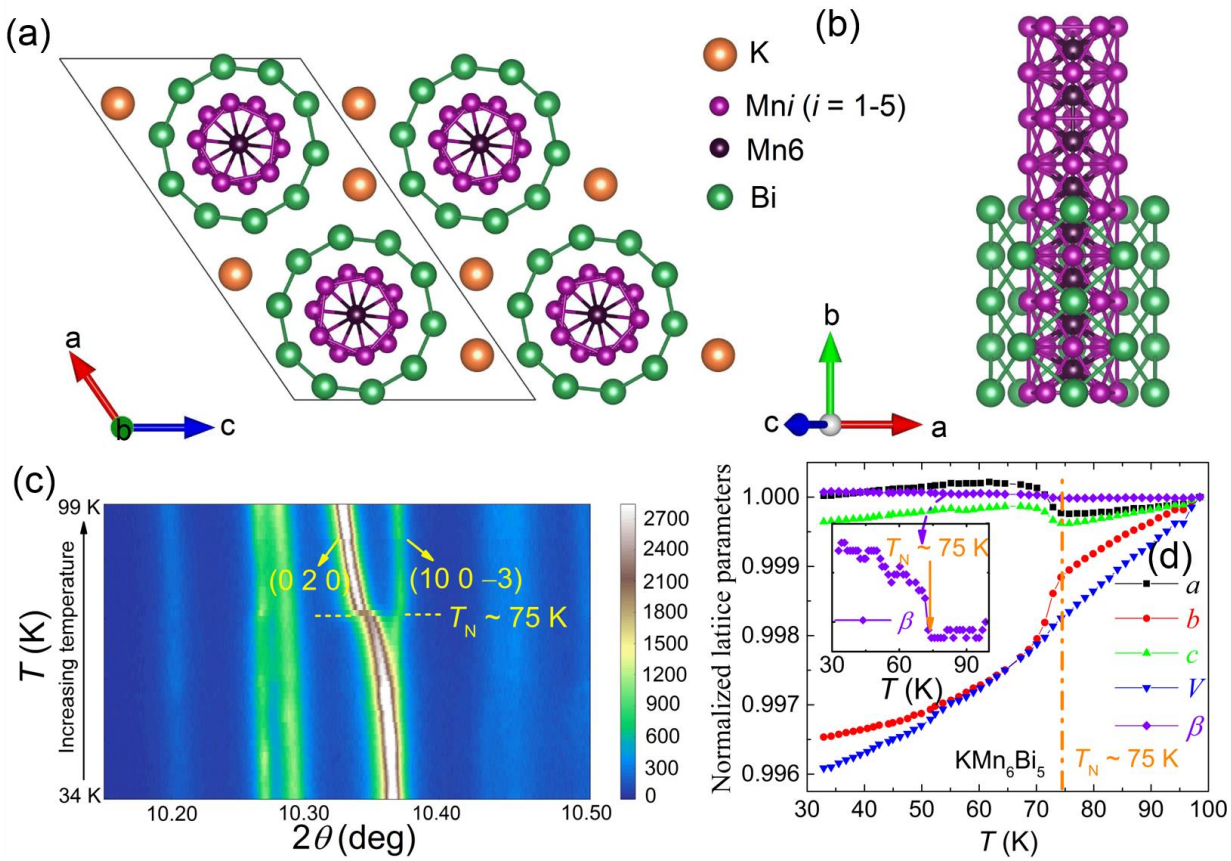

Figure 1 (a) Top view of the crystal structure of KMn_6Bi_5 down the *b* axis. The bonds were added to help present the nanowire structure of $[Mn_6Bi_5]^-$ more clearly. (b) The structural configuration of the Bi nanotube and the Mn cluster chain in the $[Mn_6Bi_5]^-$ nanowire along the *b*-axis direction. (c) Temperature-dependent powder x-ray diffraction of KMn_6Bi_5 in a selected range of diffraction angles. (d) Temperature-dependent normalized lattice parameters of KMn_6Bi_5. The inset is a magnified view around the phase transition of the monoclinic angle β. The orange dash dot line is a guide to the eye.

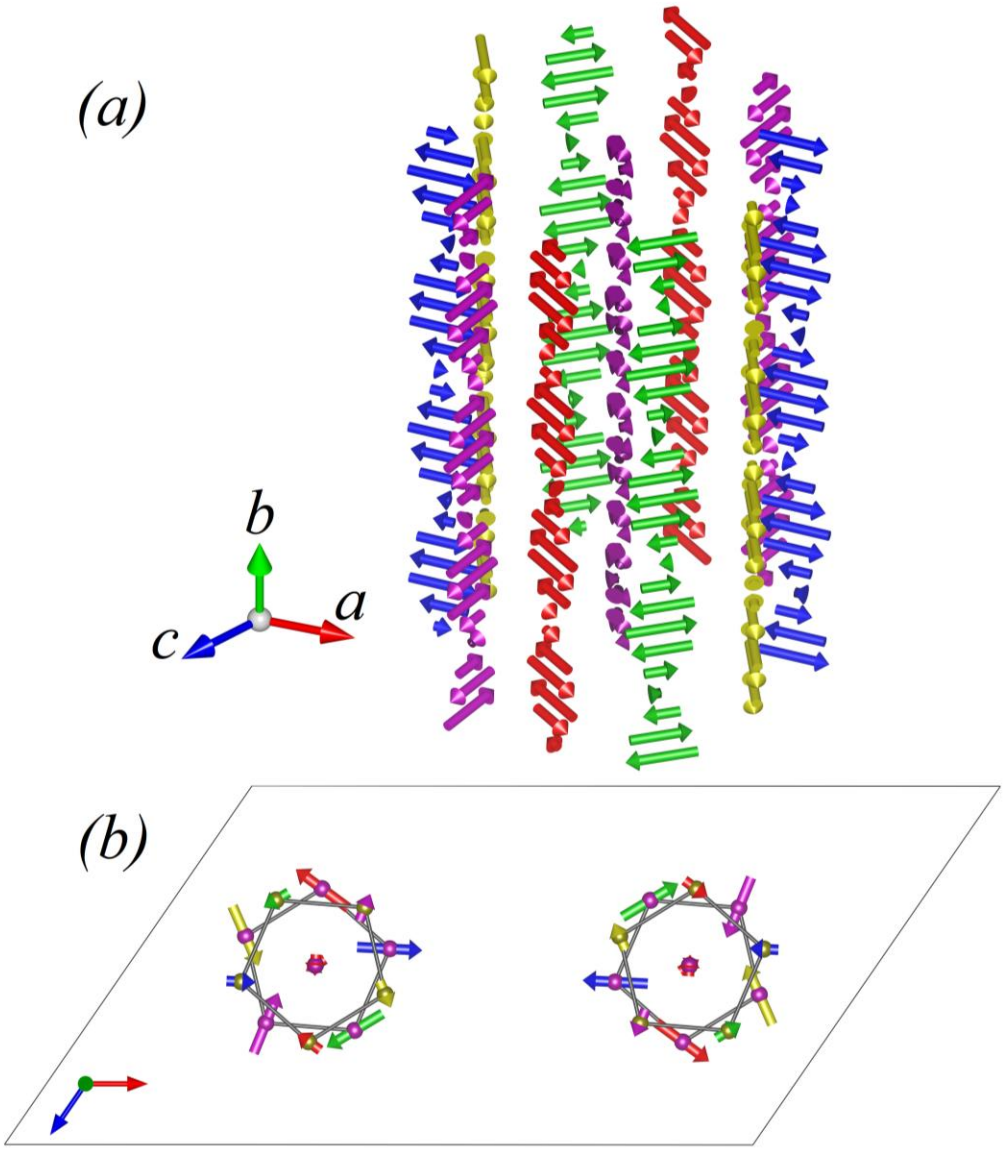

Figure 2 (a) Incommensurate spin density wave (ISDW) magnetic structure of KMn_6Bi_5. The structure is plotted over 25-unit cells stacked along the *b*-axis. The unit cell's *b*-parameter is significantly compressed to help visualize the waves over many unit cells. Waves passing through both Mn pentagons are shown together with the chain Mn (purple) through the pentagons' axis. (b) A [010] view of the base unit cell showing the two Mn pentagons (purple spheres at y = 0; dark yellow spheres at y = 0.5). Arrows of the same color are located on two Mn sites that are symmetry related by *C*-centering. Detailed views are shown in Figure 3. See text for more details.

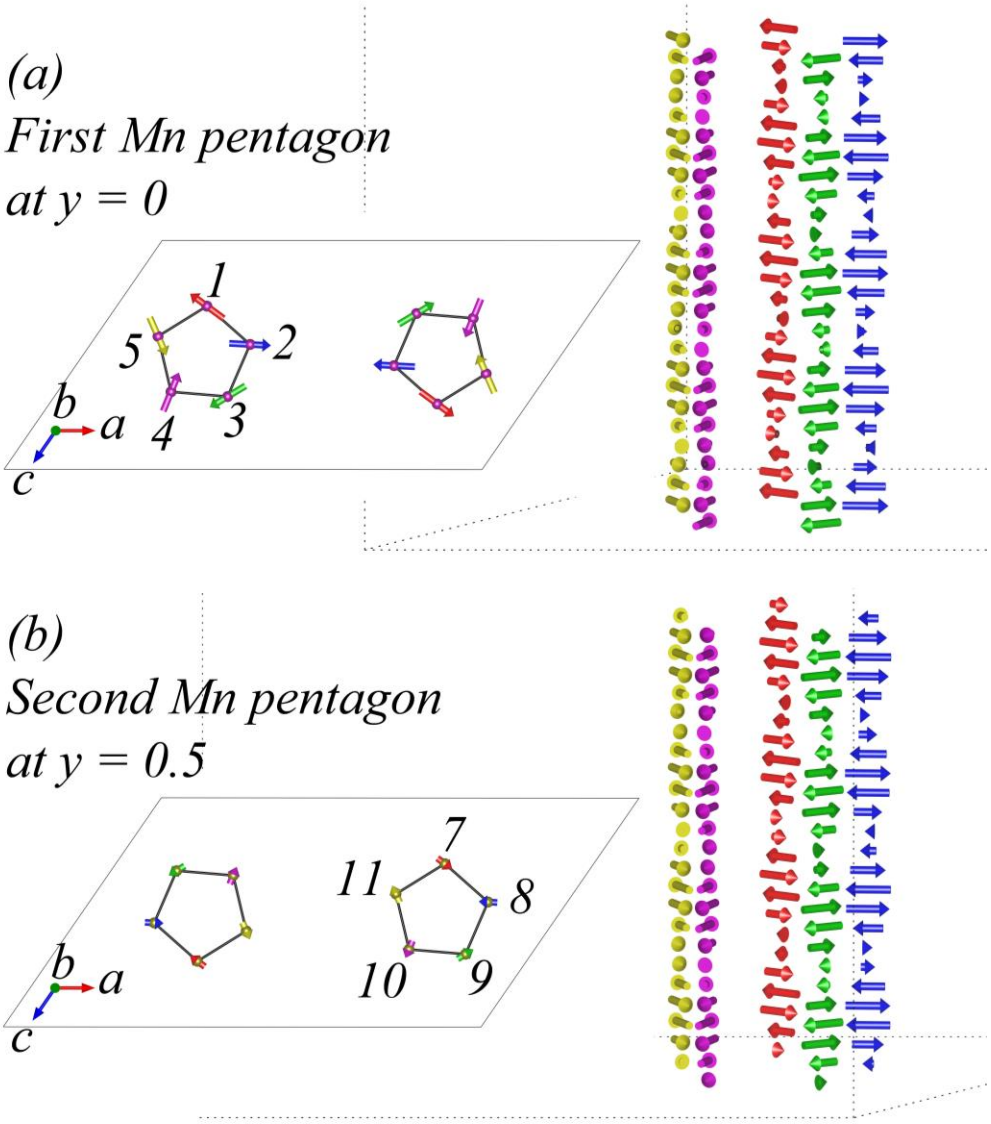

Figure 3 ISDWs passing through (a) the first Mn pentagon located at $y = 0$ as shown to the left of the figure and (b) the second pentagon located at $y = 0.5$. Notice the AFM coupling along the wave propagation direction and that the sublattices are being out-of-phase (See text for more details).

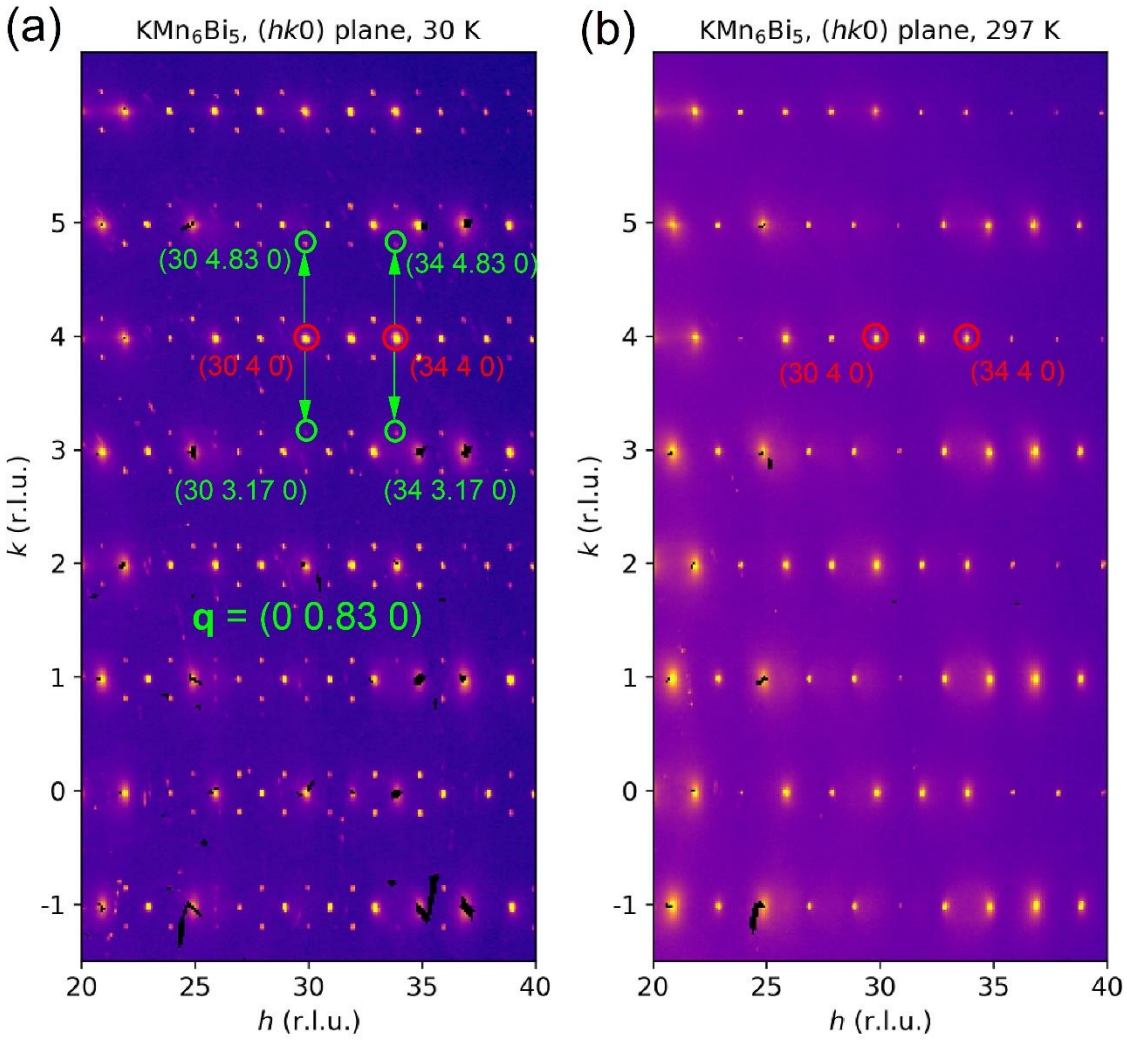

Figure 4. Integrated synchrotron x-ray diffraction intensities measured in the (*hk*0) plane for KMn_6Bi_5 at (a) 30 K and (b) 297 K, respectively. Examples of CDW satellite peaks and their corresponding **q**-vector are present.

Supplemental Material:
Spin and charge density waves in the quasi-one-dimensional KMn_6Bi_5

Jin-Ke Bao[1,2,3], Huibo Cao[4], Matthew J. Krogstad,[1,5] Keith M. Taddei[4], Chenfei Shi[2], Shixun Cao[2,3], Saul H. Lapidus[5], Sander van Smaalen[6], Duck Young Chung[1], Mercouri G. Kanatzidis[1,7], Stephan Rosenkranz[1], Omar Chmaissem[1,8,*]

[1]*Materials Science Division, Argonne National Laboratory, Lemont, Illinois 60439, USA*

[2]*Department of Physics, Materials Genome Institute and International Center for Quantum and Molecular Structures, Shanghai University, Shanghai 200444, China*

[3]*Shanghai Key Laboratory of High Temperature Superconductors, Shanghai University, Shanghai 200444, China*

[4]*Neutron Scattering Division, Oak Ridge National Laboratory, Oak Ridge, Tennessee 37831, USA*

[5]*Advanced Photon Source, Argonne National Laboratory, Lemont, Illinois 60439, USA*

[6]*Laboratory of Crystallography, University of Bayreuth, Bayreuth 95447, Germany*

[7]*Department of Chemistry, Northwestern University, Evanston, Illinois 60208, USA*

[8]*Department of Physics, Northern Illinois University, DeKalb, Illinois 60115, USA*

*Corresponding author: chmaissem@anl.gov

Experimental Methods

Single crystals of KMn_6Bi_5 were grown using excess flux of bismuth as described by Bao et al. [1]. KMn_6Bi_5 polycrystalline samples were first prepared by a conventional solid-state reaction. A precursor with the composition "Mn_6Bi_5" was synthesized by heating a mixture of Mn and Bi powders at 673 K for 24 h in an evacuated fused-silica tube. The precursor was then ground into fine powder, mixed with small pieces of K metal in the nominal composition ratio of $K_{1.03}Mn_6Bi_5$, loaded into an alumina crucible and sintered at 573 K for 12 h in an evacuated fused-silica tube. The sintered mixture was thoroughly ground and reannealed at 803 K for 24 h. The same procedure was repeated at 743 and 658 K to ensure the high-quality of a homogeneous KMn_6Bi_5 polycrystalline phase.

For synchrotron powder x-ray diffraction, powder sample of KMn_6Bi_5 was mixed with amorphous SiO_2 in the molar ratio of 1:25 and sealed in an evacuated quartz capillary. This diluting step was necessary to minimize the sample's high x-ray absorption. Temperature-dependent data, between 34 and 99 K, were collected while ramping at a constant rate at beamline 11-BM-B of the Advanced Photon Source at Argonne National Laboratory (ANL). Measurements were performed with a radiation wavelength of 0.41 Å. Repeated scans of the same angular range were continuously carried out at an interval of 1.5 K. Contour plots of the temperature-dependent data were created using the software package GSAS-II [2]. Lattice parameters were extracted from Rietveld refinements using the software package suite GSAS/EXPGUI [3,4].

Large three-dimensional volumes of single crystal diffraction were measured at beamline 6-ID-D of the Advanced Photon Source at 30 and 297 K. Data were collected using an x-ray energy of 87 keV with the sample continuously rotating over 360° at a rate of 1 degree per second while a Pilatus 2M CdTe area detector collected images at a 10 Hz rate. The temperature was controlled with an N-Helix Cryocooler at 30 K while the sample was in a dry N-stream at RT.

Magnetic structure determination and order parameter scans were performed using neutron powder diffraction at beamline HB-2A and neutron single crystal diffraction at beamline HB-3A [5] at the high flux isotope reactor (HFIR) at Oak Ridge National Laboratory (ORNL). Integrated intensities of 344 nuclear and 238 magnetic reflections were collected at 4 K using a two-dimensional camera "Anger" [5] that allows for the rapid registration and integration of multiple rocking curves. Solution of the incommensurate magnetic structure was obtained using

BasIreps [6] together with the simulated annealing procedure and Rietveld refinement methods as implemented in Fullprof [7].

Magnetic Structure Modeling

Analysis of the magnetic reflections collected at 4 K reveals the breakdown of the *C*-centering of the host nuclear lattice for a magnetic structure although no strong reflections violating the centering have been observed because symmetry constraints imposed on the Mn pentagons by a *C*-centered magnetic lattice (six independent sites) result in unsatisfactory agreement factors on the order of ~27%. Removing the *C*-centered magnetic cell results in twelve independent Mn sites and the refinements quickly converged to a solution of an antiferromagnetic spin density wave with the propagation vector along the *b*-axis with a goodness-of-fit agreement factor of about 8%, see Figure S2(b).

The theoretical models [8] of possible commensurate magnetic structures were constructed with significant constraints imposed suggesting that the magnetic structure is likely helical with a propagation vector in the direction of the *b*-axis. In contrast, our model was determined with the Mn magnetic moments free to orient in any direction within the *ac* planes. Canting of the moments in the direction of the *b*-axis was attempted but ultimately dismissed because the angles that resulted from the refinements were small within two or three standard deviations for the current dataset to resolve. Refinements using spiral helical magnetic structures were not successful. Elliptical helical models, on the other hand, always converged to our final solution of a spin-density-wave structure.

When allowed to refine independently, maximum wave amplitudes of ~2.45 to 2.55 μ_B were obtained for the Mn atoms making the pentagons. The central Mn atoms (*i.e.*, Mn6 and Mn12 sandwiched between two different pentagons) have small, refined amplitudes of less than 0.5 μ_B with relatively large standard deviations because their contributions to the magnetic scattering are much smaller than the Mn atoms in the pentagons. The magnetic moments of the central Mn atoms are favored to be aligned in the *ac* plane as the case in the Mn pentagons. The magnetic moment size for each Mn atoms in the pentagon remains more or less the same. In the final refinements, the amplitudes of the five pentagon Mn atoms were constrained to be all equal and their phases

are set to the same within one pentagon. Despite the constrained amplitudes, the magnetic moments were free to rotate in any direction within the *ac* planes. The breaking of C-centering does not restrict the directions of magnetic moments of two independent pentagons to be symmetry-related. The refinement always leads to almost a colinear configuration for the symmetry-related Mn atoms from C-centering. In our final model, we restricted those magnetic moments and the agreement factor does not increase. The net magnetic moments (~0.3 μ_B/pentagon as the amplitude) from the Mn pentagons in SDWs are not totally cancelled out.

Table S1 Refined parameters of the nuclear structure at 4 K for a KMn_6Bi_5 single crystal. Monoclinic space group *C*2/m with lattice parameters a = 22.8560 Å, b = 4.5565 Å, c = 13.3193 Å, $\alpha = 90^o$, $\beta = 124.55^o$, $\gamma = 90^o$. Unit cell volume = 1168.7449 $Å^3$. Number of effective reflections with $I > 1.00$ sigma: 344. Residual agreement factors: R_I = 2.25%, wR_I = 3.45%, R_F = 1.90% and χ^2: 3.87.

Atom	Wyckoff Position	*x*	*y*	*z*	B ($Å^2$)
K	4*i*	0.8689(2)	0	0.1148(3)	0.68(8)
Mn1	4*i*	0.1884(2)	0	0.2868(3)	0.40(8)
Mn2	4*i*	0.3341(2)	0	0.4540(3)	0.42(8)
Mn3	4*i*	0.6375(2)	0	0.3184(3)	0.24(7)
Mn4	4*i*	0.2373(2)	0	0.6611(3)	0.25(7)
Mn5	4*i*	0.1299(2)	0	0.4189(3)	0.35(8)
Mn6	4f	0.25	0.25	0.5	0.30(8)
Bi1	4*i*	0.63406(8)	0	0.1069(1)	0.25(4)
Bi2	4*i*	0.09466(8)	0	0.5866(1)	0.29(4)
Bi3	4*i*	0.04062(8)	0	0.1637(1)	0.29(4)
Bi4	4*i*	0.27714(8)	0	0.2063(1)	0.32(4)
Bi5	4*i*	0.52477(7)	0	0.3447(1)	0.23(4)

Table S2 SDW magnetic model for KMn_6Bi_5 at 4 K. The propagation vector (-1, -0.418, 0) is used for the refinements. The magnetic moments on the Mn sites are described by a spherical coordination (R, θ, φ). The *x*-axis is along the *a*-axis and the *y* axis is along the *b*-axis of the crystal structure. The *z*-axis is determined by *x* and *y* axes using the right-hand rule. The magnetic moments are in the *ac* plane (φ = 0). The crystal structure symmetry and its corresponding magnetic symmetry are as follows:
SYMM X, Y, Z MSYM u,v,w, 0.00
SYMM -X+1,Y,-Z+1 MSYM -u,v,-w, 0.00

Atom	Amplitude (R) (μ_B)	Theta (θ) (degree)	Phi (φ) (degree)	Phase of waves (2π)
Mn1	2.46	-126	0	0 (fixed)
Mn2	2.46	87	0	0 (fixed)
Mn3	2.46	-59	0	0 (fixed)
Mn4	2.46	158	0	0 (fixed)
Mn5	2.46	24	0	0 (fixed)
Mn6	0.29	-58	0	0.96
Mn7	2.46	-126	0	0.29
Mn8	2.46	87	0	0.29
Mn9	2.46	-59	0	0.29
Mn10	2.46	158	0	0.29
Mn11	2.46	24	0	0.29
Mn12	0.29	-183	0	0.1

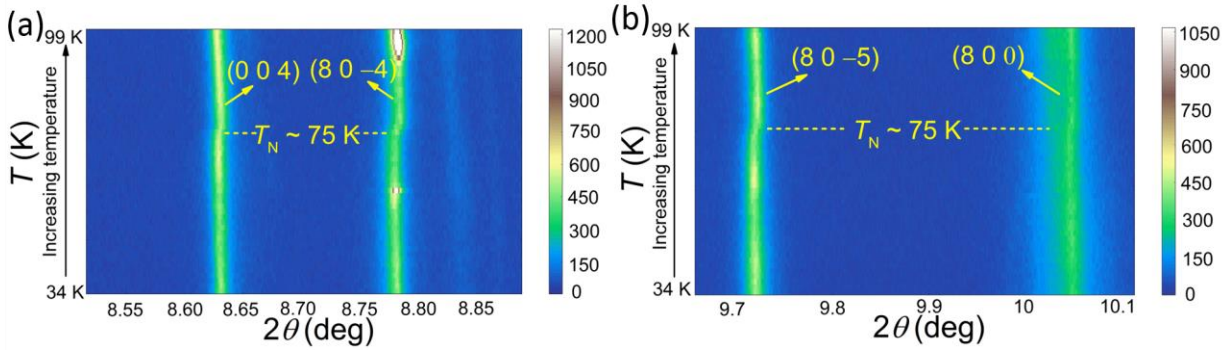

Figure S1 (a) (b) Temperature-dependent powder x-ray diffraction of KMn_6Bi_5 in a selected range of diffraction angles. The relevant reflections (8 0 -5), (8 0 0), (0 0 4) and (8 0 -4) were tracked across the phase transition T_N. The dashed lines are a guide to the eye.

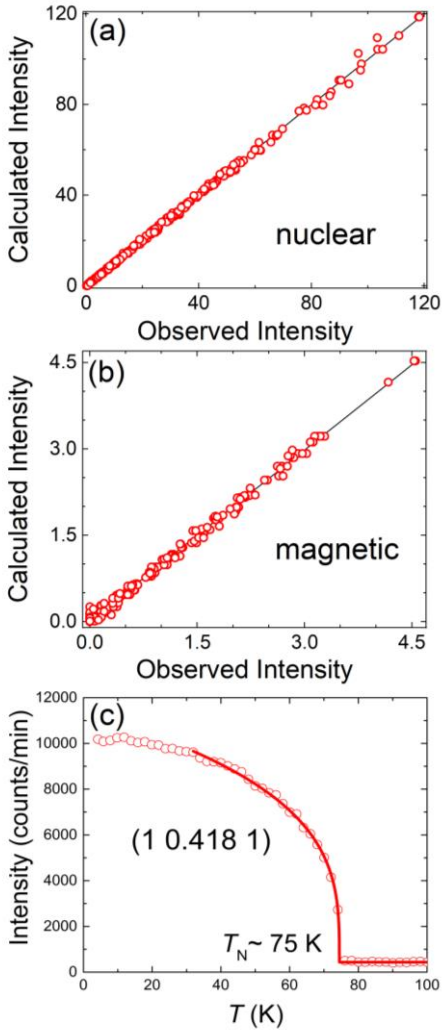

Figure S2 The relationship between the observed and calculated reflection intensity for refined nuclear (a) and magnetic (b) structures from single crystal neutron diffraction. The data points are almost located on the straight line, indicating an excellent fit. (c) Temperature-dependent integrated intensity of the magnetic reflection (1 0.418 1) from single crystal neutron diffraction. The red line is the fit of the critical behavior near the phase transition. It can be well fitted using a standard power-law equation $I = I_0 + I_M(1 - \frac{T}{T_N})^{2\beta}$ as described by Chatterji et. al. [9] and Karna et al. [10]. Here, I_0 is a temperature-independent term arising mainly from noise background of detector, I_M reflects magnetic contributions at 0 K, T_N is the magnetic phase transition temperature and β is the critical exponent. The fitted value of T_N = 74.5(3) K is fully consistent with the anomaly observed in the x-ray diffraction data and the phase transition reported by Bao *et al.* [1].

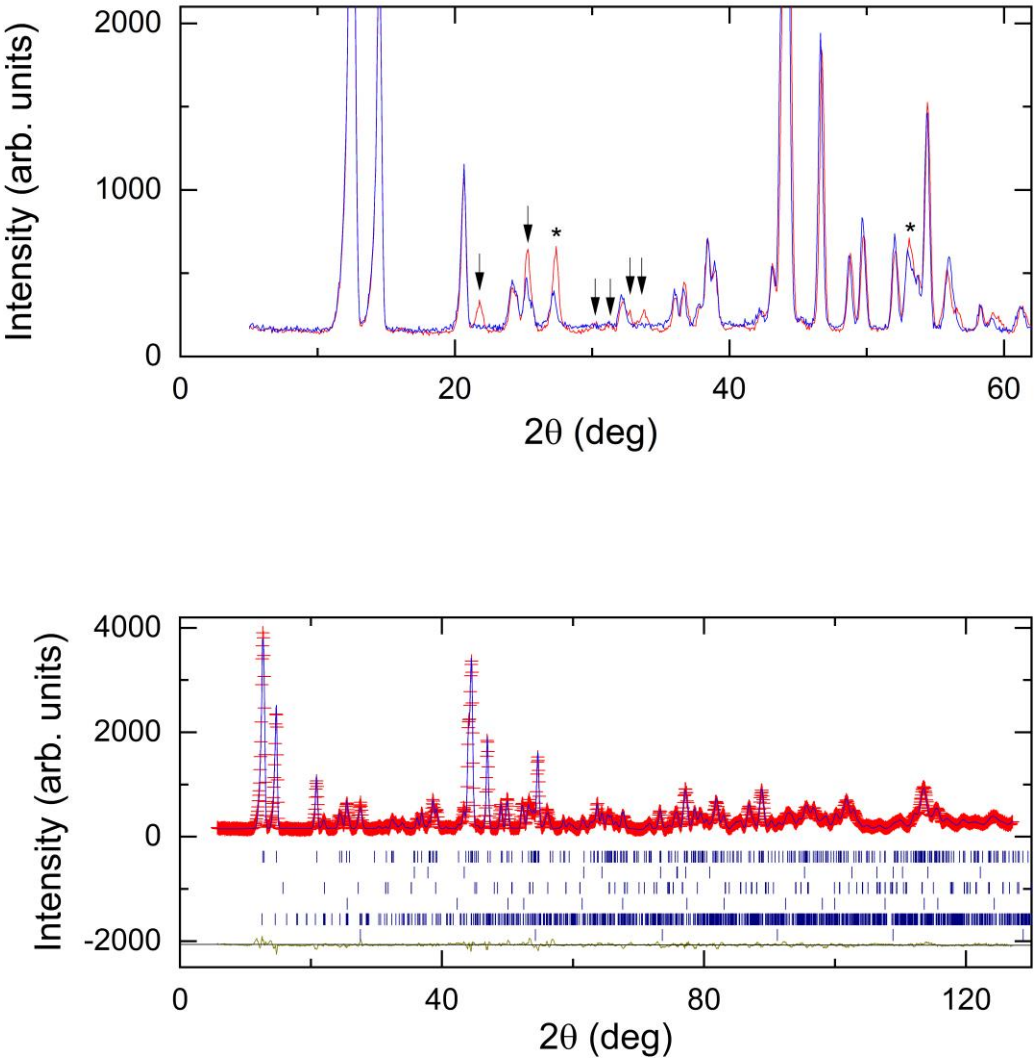

Figure S3. Neutron Powder Diffraction. (a) Raw data collected at 3 K and 297 K, highlighting the magnetic peaks of KMn_6Bi_5 (arrows) that appear below 75 K. Two magnetic peaks that belong to a tiny impurity phase MnO are also observed (asterisks). (b) Best-fit Rietveld refinements of the nuclear and magnetic structure of KMn_6Bi_5. Observed intensities, calculated intensities, and the difference plot are represented by plus symbols (+), a solid blue line, and a solid dark yellow line, respectively. Tick marks (from top to bottom) indicate the Bragg positions of the nuclear reflections of KMn_6Bi_5, Bi, MnO, KBi_2, and the magnetic reflections of KMn_6Bi_5 and MnO. Weight Fractions for KMn_6Bi_5: 92.8(9)%, Bi: 3.24(2)%, MnO: 1.07(4), KBi_2: 2.95(12).

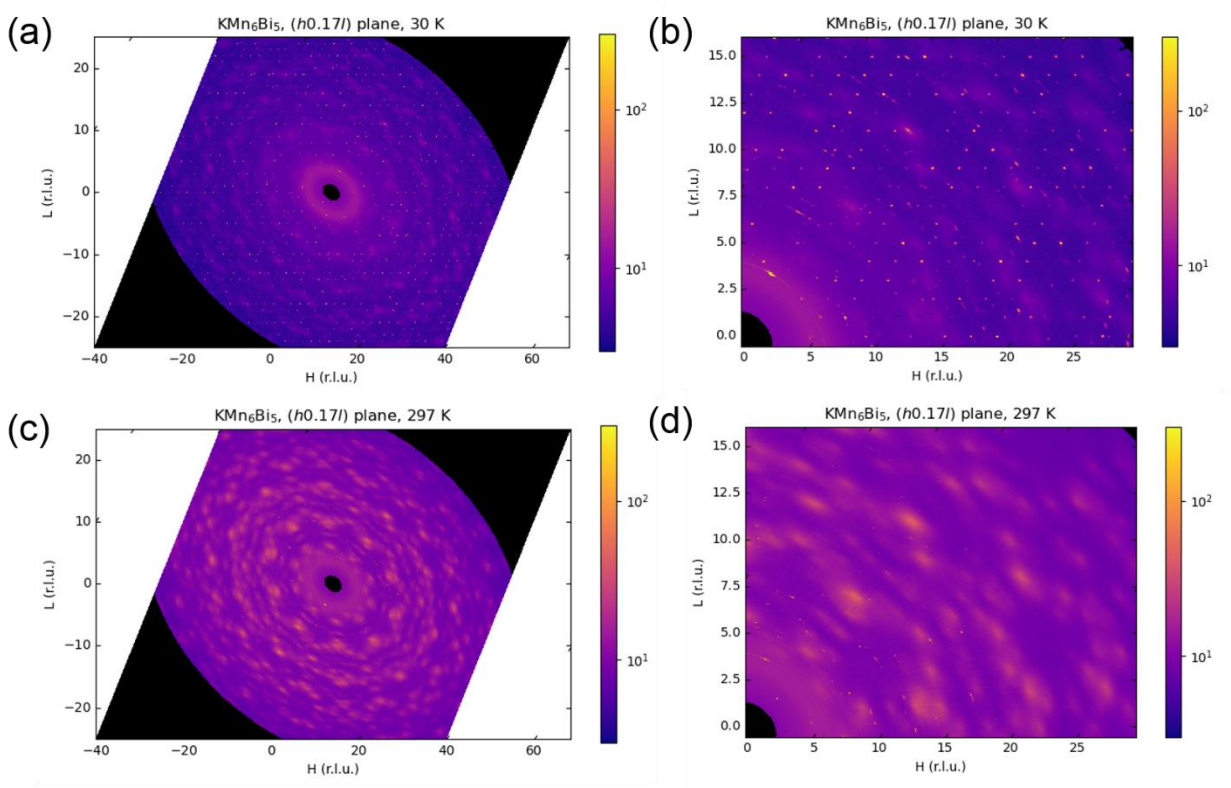

Figure S4 (a), (c) Integrated synchrotron x-ray scattering intensities of (*h*1.17*l*) planes at 30 and 297 K, respectively. (b) and (d) are the corresponding zoomed plots for (a) and (c), respectively. Satellite peaks are well resolved at 30 K in a wide reciprocal space while they are absent at 297 K

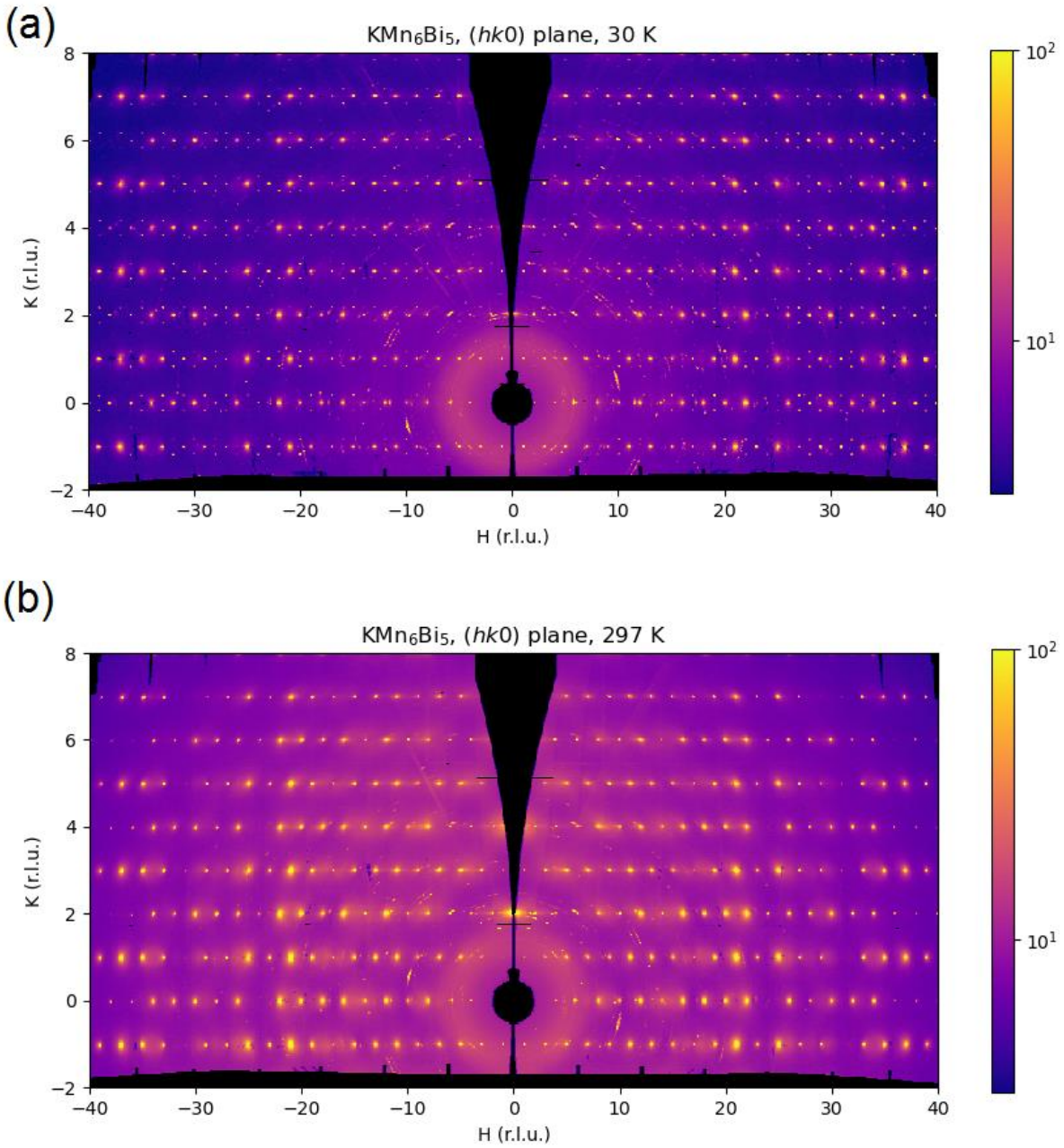

Figure S5 (a), (b) Integrated synchrotron x-ray scattering intensities of (*hk*0) planes in a wide reciprocal space at 30 and 297 K, respectively. The satellite peaks are well resolved at 30 K while they are absent at 297 K.

Supplemental References

[1] J.-K. Bao, Z.-T. Tang, H. J. Jung, J.-Y. Liu, Y. Liu, L. Li, Y.-K. Li, Z.-A. Xu, C.-M. Feng, H. Chen, et al., *Unique [Mn_6Bi_5]$^-$ Nanowires in KMn_6Bi_5: A Quasi-One-Dimensional Antiferromagnetic Metal*, J Am Chem Soc **140**, 4391 (2018).

[2] B. H. Toby and R. B. von Dreele, *GSAS-II: The Genesis of a Modern Open-Source All Purpose Crystallography Software Package*, J Appl Crystallogr **46**, 544 (2013).

[3] Larson A. C. and R. B. von Dreele, *General Structure Analysis System (GSAS); Los Alamos National Laboratory Report LAUR 86-748*, Los Alamos National Laboratory: Los Alamos, NM, (2004).

[4] B. H. Toby, *EXPGUI, a Graphical User Interface for GSAS*, J Appl Crystallogr **34**, 210 (2001).

[5] H. Cao, B. Chakoumakos, K. Andrews, Y. Wu, R. Riedel, J. Hodges, W. Zhou, R. Gregory, B. Haberl, J. Molaison, et al., *DEMAND, a Dimensional Extreme Magnetic Neutron Diffractometer at the High Flux Isotope Reactor*, Crystals (Basel) **9**, 5 (2018).

[6] J. Rodriguez-Carvajal, *BASIREPS: A Program for Calculating Irreducible Representations of Space Groups and Basis Functions for Axial and Polar Vector Properties*, Solid State Phenom **170**, (2011).

[7] J. Rodríguez-Carvajal, *Recent Advances in Magnetic Structure Determination by Neutron Powder Diffraction*, Physica B Condens Matter **192**, 55 (1993).

[8] L. Chen, L. Zhao, X. Qiu, Q. Zhang, K. Liu, Q. Lin, and G. Wang, *Quasi-One-Dimensional Structure and Possible Helical Antiferromagnetism of $RbMn_6Bi_5$*, Inorg Chem **60**, 12941 (2021).

[9] T. Chatterji, *Neutron Scattering from Magnetic Materials* (Elsevier, Amsterdam, 2006).

[10] S. K. Karna, D. Tristant, J. K. Hebert, G. Cao, R. Chapai, W. A. Phelan, Q. Zhang, Y. Wu, C. Dhital, Y. Li, et al., *Helical Magnetic Order and Fermi Surface Nesting in Noncentrosymmetric ScFeGe*, Phys Rev B **103**, 014443 (2021).